Journal of Rock Mechanics and Geotechnical Engineering 18 (2026) 3688–3702

Contents lists available at ScienceDirect

Journal of Rock Mechanics and Geotechnical Engineering

journal homepage: www.jrmge.cn

Full Length Article

Mechanical behavior of mixed rock-ice deposits in high-latitude mountainous areas

Wenbin Chang [a,b], Aiguo Xing [a,*], Changbao Guo [c,**], Wenbo Zhao [c]

[a] State Key Laboratory of Ocean Engineering, Shanghai Jiao Tong University, Shanghai, 200240, China
[b] Department of Civil Engineering, Monash University, Melbourne, VIC, 3800, Australia
[c] Institute of Geomechanics, Chinese Academy of Geological Sciences, Beijing, 100081, China

ARTICLE INFO

Article history:
Received 20 February 2025
Received in revised form
3 June 2025
Accepted 3 June 2025
Available online 18 September 2025

Keywords:
Rock-ice mixtures
Ice melting
Triaxial testing
Thermodynamic behavior
Secondary disasters

ABSTRACT

The mixed rock-ice deposits in high-latitude areas usually come from the accumulation of rock-ice avalanches. Melting tests and temperature-controlled triaxial tests were conducted on rock-ice mixture samples with varying volumetric ice contents (0.25, 0.5, and 0.75), environment temperatures (0.5 °C, 1 °C, and 1.5 °C), and temperature control durations (20 min, 40 min, and 60 min), aiming to investigate the thermodynamic behavior of rock-ice mixed deposits under an ablation environment. Our findings reveal that the melting behavior of rock-ice mixtures mainly occurs in the surface layer; then, ice meltwater transports along the surface seepage path to the bottom of the sample. Notably, the basal meltwater gathering zone leads to accelerated melting of the ice debris, and the cohesion and occlusion between the rock debris in this zone almost disappear, ultimately resulting in severe basal damage. Triaxial test results indicate that the basal damaged zone leads to an easy initial compression process of the rock-ice mixture samples and forms a basal strain effect. Statistics show that ice content, environment temperature, and temperature control duration all show a negative impact on the mixture's peak strength in thaw environments, which also exacerbates the basal strain effect, with a maximum basal strain of 8.61% and a corresponding mass loss ratio of 28.69%. Finally, the mechanisms of the secondary sliding of the mixed deposits and the failure mode of the rock-ice deposit dams induced by ice debris melting were discussed.

© 2026 Institute of Rock and Soil Mechanics, Chinese Academy of Sciences. Published by Elsevier B.V. This is an open access article under the CC BY-NC-ND license (http://creativecommons.org/licenses/by-nc-nd/4.0/).

1. Introduction

Rock-ice avalanches are a large-scale geologic hazard in the region of alpine glaciers caused by ice avalanches or rock collapses (Deline et al., 2021; Leinss et al., 2021; Zhang et al., 2023a). Since the 21st century, global warming has led to accelerated glacier melting and frequent glacier avalanches, and rock-ice avalanches of different magnitudes have been widely reported. Relevant studies show that these rock-ice avalanche hazards were mainly concentrated in the European Alps (Faillettaz et al., 2011, 2015; Fischer et al., 2013), the Alaskan mountains (Lipovsky et al., 2008; Jacquemart et al., 2020), the Caucasus (Huggel et al., 2005), the Andes (Falaschi et al., 2019), and the high mountainous regions of Asia (van der Woerd et al., 2004; Kääb et al., 2018, 2021; Gnyawali et al., 2020; Fan et al., 2022; Chang and Xing, 2025a), and some of these events resulted in severe casualties and economic losses. When rock-ice avalanches occur, the ice and rock mass detached from the starting zone will have an entrainment effect on the materials along its propagation path (Pudasaini and Krautblatter, 2021; Pudasaini, 2022), ultimately forming fluidized mixtures of rock-ice debris accumulated in the gully and the valley (Schneider et al., 2011; Sosio, 2015; Chang and Xing, 2025b). The complex dynamics of rock ice avalanches, such as ice melting, base erosion, base lubrication, and internal fluidization, make rock ice-avalanche deposits a multiphase mixture (Pudasaini and Krautblatter, 2014; Pudasaini, 2024). As this powerful mixing mass flow meets the river downstream, it can accumulate at the confluence and block the river, forming a rock-ice avalanche deposit dam and the barrier lake (Shang et al., 2003;

* Corresponding author.
** Corresponding author.
E-mail addresses: xingaiguo@sjtu.edu.cn (A. Xing), guochangbao@cags.ac.cn (C. Guo).

Peer review under responsibility of Institute of Rock and Soil Mechanics, Chinese Academy of Sciences.

https://doi.org/10.1016/j.jrmge.2025.06.041
1674-7755/© 2026 Institute of Rock and Soil Mechanics, Chinese Academy of Sciences. Published by Elsevier B.V. This is an open access article under the CC BY-NC-ND license (http://creativecommons.org/licenses/by-nc-nd/4.0/).

Yin and Xing, 2012; Fan et al., 2022). Although the rock-ice avalanche hazards are well known, the mixed rock-ice deposits and dams formed by the rock-ice avalanches are likely to form secondary disasters in a thaw environment. Specifically, ice or snow debris inside the deposits will melt with rising ambient temperatures, and the meltwater can significantly affect the mechanical properties of the mixtures.

Current reports about rock-ice avalanche deposit-induced secondary hazards cover mainly rock-ice mixed dam failure (Borgatti et al., 2006; Kropáček et al., 2021; Fan et al., 2021; Zhang et al., 2023b). For example, due to the increasing average annual temperature and receding glaciers, the Amney Machen Mountains located in the eastern Tibetan Plateau, China, have experienced four significant rock-ice avalanche events during the past 20 years (Paul, 2019; Kääb et al., 2021; Zhang et al., 2023b). According to Zou et al. (2023), the Amney Machen rock-ice avalanche produced about 15.7×10^6 m^3, 5.9×10^6 m^3, 3.5×10^6 m^3, and 0.6×10^6 m^3 of deposits in 2004, 2007, 2016, and 2019, respectively. The field investigation performed in 2004 about the Amney Machen case showed that the main composition of the deposits was a mixture of rock debris and ice debris, with a portion of ice meltwater (Fig. 1a). The volumetric ice content of the deposits is about 80%, with an ice fragment size range from 0.05 to 0.25 m, except for a few ice debris with sizes of 1–6 m (Fig. 1c). After the Amney Machen rock-ice avalanche occurred in 2004, the rock-ice deposits formed a dam in the Qushian River, with a width of about 200 m, an average height of about 10 m, and a volume of about 1.1×10^6 m^3 (Fig. 1b). A large number of subsidence cracks, sinkholes, and localized collapses have formed on the dam body due to the surface ice melting and settlement of the deposits. In the field, there found some cracks in the dam, the largest one with a length of 60–80 m, a width of 0.2–2 m, and a depth of 1–3 m (Fig. 1d). Ice melt water develops a large number of seepage channels within the dam and eventually flows into the river at the bottom of the dam.

In the future, along with glacier melting, large-scale rock-ice avalanches in this region could remain possible, producing large volumes of rock-ice deposits. The recent rock-ice avalanche that occurred in Chamoli, India in February 2021 has once again attracted much attention worldwide. In this case, mixing the material flow of ice and rock moving at a high speed, blocked the river in the valley and formed a deposit dam with a volume of about 8×10^6 m^3 (Kropáček et al., 2021; Siddique et al., 2022). According to Shugar et al. (2021), the rock-ice mixtures dam destabilized only a few hours later, causing a supermassive flood with a mean discharge of about 8200–14200 m^3/s. Wang et al. (2024) suggest that the rapid failure of the dam in the Chamoli case was not only related to the rapid rise in the lake level but that the large number of ice blocks inside the dam was also accountable. Similar rock-ice deposit dam failure events also occurred in several famous rock-ice avalanches, such as the Yigong case in 2000 (Delaney and Evans, 2015; Kang et al., 2017), the Kolka Karmadon case in 2002 (Huggel et al., 2005), and the Sedongpu case in 2018–2025 (Li et al., 2022, 2024; Gao et al., 2023), etc. In these events, ice meltwater played a significant role in the failure of the rock-ice mixed dams, accelerating the destruction of the dam structure. The outburst of floods that followed the dam's failure caused significant economic damage to the downstream region (Xu et al., 2012; Zhou et al., 2016). On the other hand, the reactivation of rock-ice mixture deposits under climate change conditions also cannot be ignored. Fieldwork about the Sedongpu rock-ice avalanche from An et al. (2022) shows that obvious ablation occurred in the rock-ice deposits under the intense solar radiation, causing the collapse of the deposits on both sides of the erosion grooves. Similarly, when high ice content avalanching mass accumulates in a relatively steep (15–30°) propagation area, large amounts of meltwater will affect the stability of these deposits. For this, Pudasaini (2024) has developed the full thermo-mechanical model for three-phase rock-ice avalanche dynamics with changing temperature and ice melting rate, which explains advection-diffusion of heat including the heat exchange across the rock-ice avalanche. Therefore, the thermo-mechanics and the changing temperature of the rock-ice mixtures should be considered an essential element in the security assessment of rock-ice avalanche deposits. Understanding the thermodynamic properties of rock-ice mixtures in the setting of temperature rise is crucial

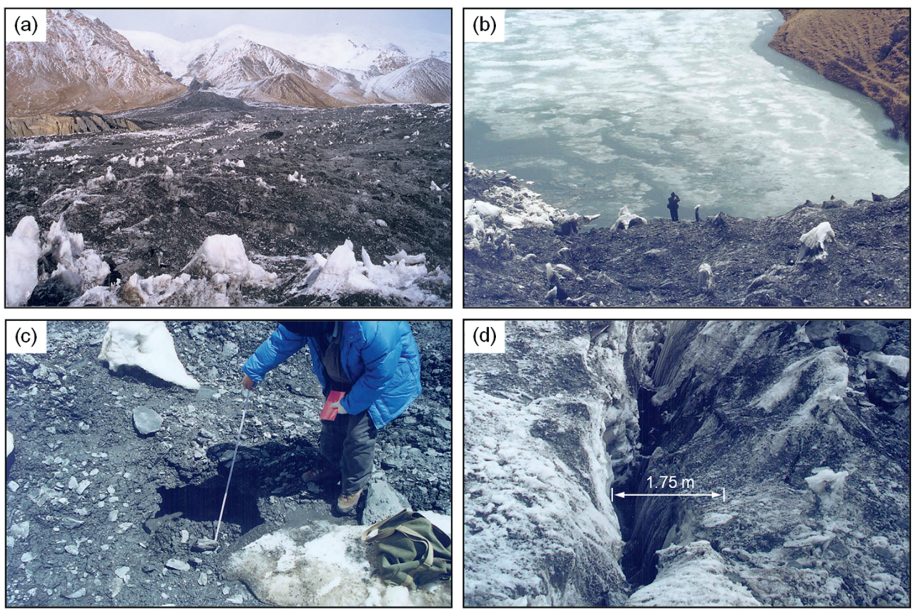

Fig. 1. Field investigation of the Amney Machen rock-ice avalanche deposits: (a) the rock-ice mixtures accumulated in the gully, (b) the rock-ice deposits dam formed in the river valley, (c) rock debris and ice debris in the deposits, and (d) the cracks formed in the deposition dam.

for revealing the deformation characteristics of rock-ice avalanche deposits and the triggering mechanisms of potential disasters. Then, the transport, mixing, and fluidization of the debris flood and the disaster chain can be simulated following the multi-phase, thermo-mechanical models (Pudasaini and Krautblatter, 2014; Pudasaini, 2024), applying for regional risk assessment.

Relevant studies have investigated the mechanical properties of rock-ice mixtures through various tests. In established studies, rock-ice mixtures exist mainly in the form of permafrost (Akagawa and Nishisato, 2009; Liu et al., 2020; Tang et al., 2023), moraines (Springman et al., 2003; Lukas, 2005), glacier basal moraines (Moore, 2014; Fitzsimons and McManus, 2001; Ladanyi, 2002), and geotechnics of other planets (Mangold et al., 2002). Existing works are more concerned with the mechanical properties of rock-ice mixtures in freeze environments, such as tensile properties, shear strength, frost heave behavior, and ice-soil interface mechanics. Only a few studies have considered the thermodynamic characteristics of rock-ice mixtures in thaw environments. In addition, volumetric ice content and ambient temperature are often cited as the key controlling factors. For instance, Krautblatter et al. (2013) analyzed the temperature dependence of shear detachment at the rock-ice interface and the mechanical destabilization process of permafrost rocks in a warming climate by direct shear tests. They found that fracture toughness, compressive, and tensile strength decrease by 50% or more when permafrost rocks are melted. Huang et al. (2023) studied the shear mechanical behavior of the ice-rich debris–rock interface at the bottom of the glacier based on temperature-controlled direct shear tests. They found that as the temperature increased from −9 °C to −1 °C, the peak and residual shear stress decreased by 62.5%–78%. Meanwhile, when the ice-rich debris-rock interface with the lowest ice content (40%), the residual shear stress is highly influenced by normal stress. From the perspective of global climate change, the thermodynamic properties of rock-ice mixtures in thaw environments need to receive more attention. As demonstrated in Fig. 2, the average annual temperatures in the RIA-prone region have been gradually increasing and exceeding the melting point of the ice, which will have a significant impact on the stability of the mixed rock-ice deposits. Focusing on the melting characteristics of ice debris and the seepage behavior of meltwater will help us understand the failure mode of rock-ice mixtures, as well as the potential geological hazards they may cause.

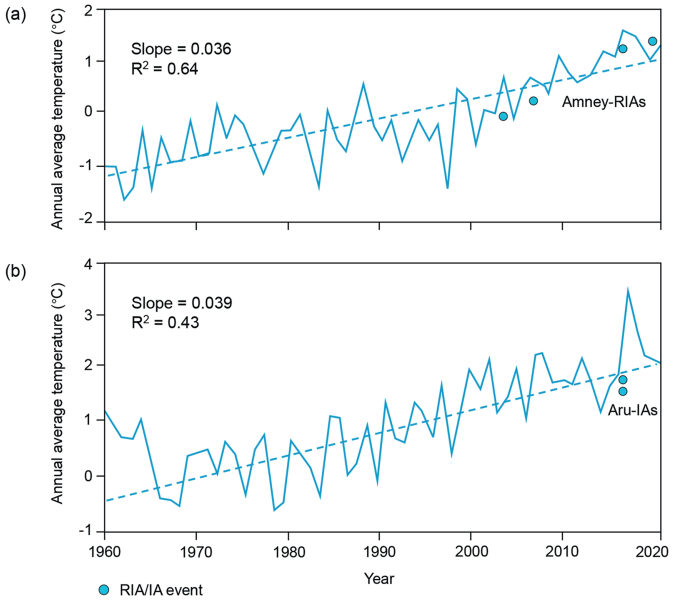

Fig. 2. The mean annual air temperature of two regions with rock-ice/ice avalanches (RIA/IA) occurred frequently in the Tibetan Plateau, China: (a) Temperature record from the Maqin Station at the eastern Tibetan Plateau. Graph modified from Zou et al. (2023). Four ice avalanche events (Amney-RIAs) occurred in the past 20 years (2004, 2007, 2016, 2019), and (b) Temperature record of the Ali region, which experienced two massive ice avalanches in 2016 (Aru-IAs). The dotted line in the graph indicates the temperature trend.

Aiming to reveal the mechanical behavior of rock-ice deposits in ablation environments and the controlling effects of different factors, sandy shale specimens collected in the field and artificial ice debris were used to conduct melting and temperature-controlled triaxial compression tests in this study. The series of test configurations in this work was derived from the field investigation results of the Amney Machen rock-ice avalanche deposits. In addition to the two commonly used control factors, volumetric ice content, and environment temperature, we added different temperature control duration conditions in the triaxial test, which is used to characterize different cycles of temperature change in the field. The melting characteristics, ice meltwater seepage behavior, and basal damage behavior of the rock-ice mixture samples under various test conditions were analyzed. According to the stress-strain characteristics and macroscopic damage patterns, a novel failure mode of the rock-ice mixtures is proposed, which clarifies the contribution of ice meltwater in mixture deformation. Furthermore, based on the experimental results, the possible mechanism of secondary hazards caused by the melting of ice debris in the rock-ice avalanche deposits is discussed.

2. Methodology

2.1. Laboratory sampling

Given the current melting status of the rock-ice avalanche deposits and the difficulty of preserving the cryogenic environment during transportation, we used remodeled samples in the laboratory to perform the test. The rock material used in the study was mainly fragmented sandy shale (Fig. 3a) collected from outcrops in the study area. The mineral composition of this sandy shale includes quartz, kaolinite, montmorillonite, illite, and mica; its physical properties are shown in Table 1. Afterward, the sandy shale blocks were pulverized into rock debris with a maximum particle size of about 5 mm (Fig. 3b). To reconstruct the characteristics of the ice rock debris in the rock-ice avalanche deposits, we selected the rock debris with a grain size between 0.2 and 5 mm, and its particle size distribution information is shown in Table 2. The ice debris required for the test was also produced in the laboratory. The pre-prepared ice blocks were crushed via an ice-crushing machine, and the ice debris was obtained (Fig. 3d–e). Owing to control conditions such as temperature and freezing duration being limited in the laboratory, there is a slight difference in strength between artificial ice debris and field ice debris (Kermani et al., 2007). In this work, the grain size distribution interval of the ice debris was controlled to be 0.5–7.5 mm (see Table 2).

When making the samples, we determined the component arrangements of the rock-ice mixtures by volumetric proportions and characterized the rock-ice proportions of the samples by their ice content (I_c). Volumetric I_c is the ratio of ice debris volume in a given sample to the total volume (Mangold et al., 2002; Arenson et al., 2004). The porosity of rock and ice debris in the compacted state was calculated, and the mass of rock and ice debris required for the samples with different I_c was determined. The porosity at five releases of the compactor was used in this study, with the porosities of rock debris and ice debris of 6.2% and 2.5%, respectively. Then, the mass of rock and ice debris required

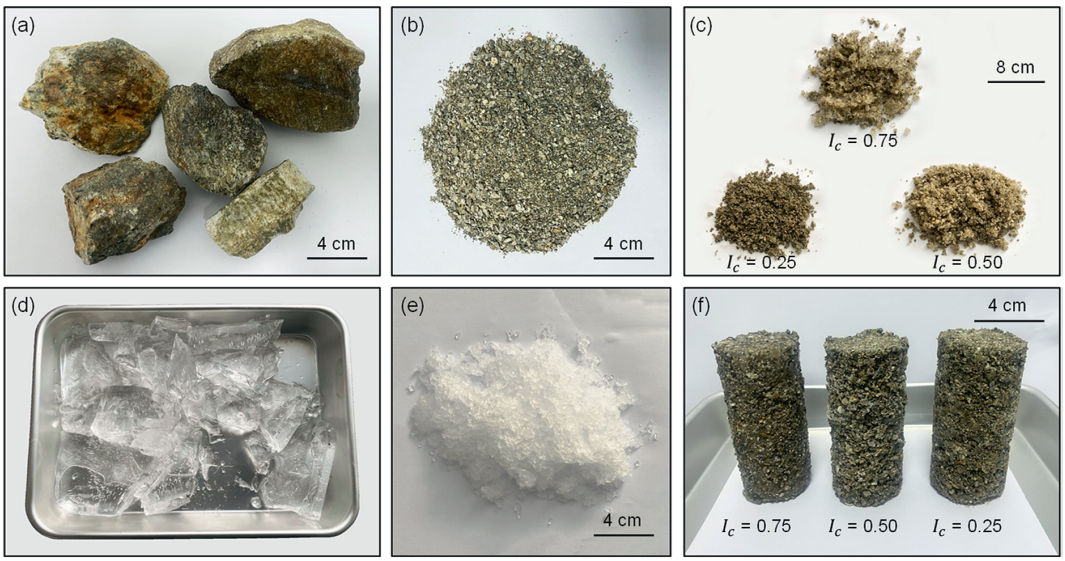

Fig. 3. Sample preparation for the tests: (a) sandy shale blocks collected from the study area, (b) sandy shale debris produced by pulverization, (c) rock-ice mixtures with different ice content, (d) ice debris made in the laboratory, (e) ice debris used in the tests, and (f) completed rock-ice mixture samples.

Table 1
Physical properties of the sandy shale used in this study.

Characteristics	Natural weight (kN/m^3)	Water content	Compressive strength (MPa)	Young's modulus (GPa)	Poisson's ratio
Sandy shale	25.65	2.34%	61.32	2.46	0.26

Table 2
Size distributions of the rock debris and ice debris.

Size interval (mm)	0.2–0.5	0.5–1	1–2	2–5	5–10
Rock debris	34.4%	27.5%	21.8%	16.3%	0%
Ice debris	0%	27.4%	19.6%	20.8%	32.2%

for different I_c samples is calculated. Information on the ice and rock debris mass fractions of the three rock-ice mixture samples is shown in Table 3. When sampling, the quantitative ice debris was quickly and evenly mixed with the rock debris and immediately placed in a cryostat for refrigeration, with the refrigeration temperature set at −4 °C. The preparation of triaxial samples was started after the rock-ice mixture was refrigerated for 30 min. Fig. 3c presents the ice rock mixtures with an ice content of 0.25, 0.5, and 0.75, respectively. The size of the triaxial test sample used in this study was 3.9 cm × 8 cm (diameter × height). During the test, the sample expands in volume after refrigeration is completed, which makes it difficult to disassemble it from the sample-making cylinder. A smooth film was placed inside the cylinder during the sample preparation process to solve this issue. The prepared triaxial sample and the sample-making cylinder were placed in a cryostat together for 48 h. The finalized samples with different ice contents are shown in Fig. 3f.

2.2. Melting test configuration

Melting tests are performed to investigate the melting characteristics of the rock-ice mixtures at different ambient temperatures. In this work, 0.5 °C and 1 °C two temperature conditions were designed. The temperature conditions of the melting test are implemented by a temperature control box with a temperature control accuracy of 0.1 °C. Before performing the melting test, set the target temperature and quickly place the samples in the box after the temperature has stabilized. Water barrier paper was placed at the bottom of the sample to observe the collection of meltwater. We observed the samples melting every 10 min, and the total test duration was 1 h.

2.3. Temperature-controlled undrained triaxial test configuration

The instrument used in this test was the GDS temperature-controlled triaxial apparatus (Fig. 4a–b). The test system mainly consists of the axial loading system, pressure servo system, temperature control system, digital data acquisition system, and data logger system, which provides an accurate measurement platform and advanced mechanics that can be employed over a high-stress working range, including confining pressure and back pressure (Barla et al., 2010). Specifically, the vertical load is applied to the sample using the Virtual Infinite Stiffness (VIS) loading frame. The

Table 3
Mass fractions of rock debris and ice debris for samples.

Sample ID	I_c	Sample mass (g)	Mass of rock (g)	Mass of ice (g)	Saving Temp. (°C)
RIM 1-9	0.25	195.6 ± 1.0	172.5 ± 0.5	23.3 ± 0.5	−4.0
RIM 10-18	0.50	161.6 ± 1.0	115.0 ± 0.5	46.6 ± 0.5	−4.0
RIM 19-27	0.75	127.4 ± 1.0	57.5 ± 0.5	69.9 ± 0.5	−4.0

Notes: Saving Temp. means the temperature of the environment in which the sample is saved.

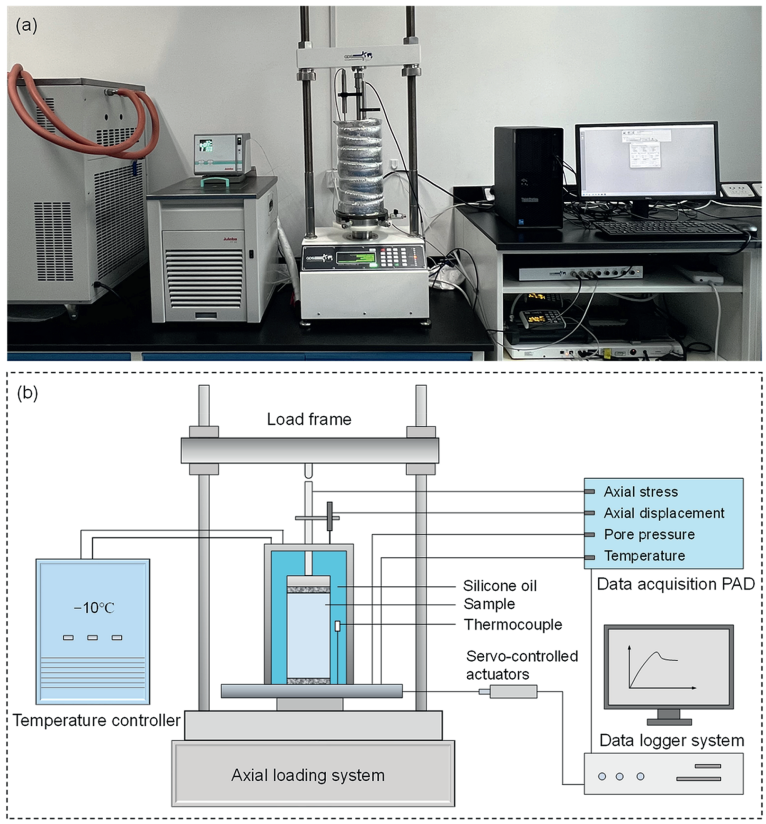

Fig. 4. Triaxial Test Configuration: (a) GDS temperature-controlled triaxial apparatus, and (b) schematic diagram of the triaxial test system.

confining pressure of the pressure chamber is applied through the silicone oil from the servo-controlled actuators (Fig. 4b). The volumetric deformation of the sample can be calculated by measuring the change in oil volume in the pressure chamber based on a hydraulic sensor. Temperature control is achieved by circulating silicone oil in a spiral tube inside the pressure chamber. A thermocouple is built into the pressure chamber to continuously measure the temperature of the silicone oil (Fig. 4b). This axial load range of the triaxial apparatus is 0–100 kN, the confining pressure range is 0–4 MPa, the axial displacement range is −50 mm to 50 mm, and the temperature control range is −20 °C to 200 °C and with an accuracy of 0.1 °C. According to the temperature data provided by the Maqin meteorological station, the annual mean air temperature in the Amney Machen mountains between 2010 and 2020 fluctuated within the range of 0.5 °C–1.5 °C, showing an increasing trend (Zou et al., 2023). The temperature levels of the pressure chamber were set in the test with 0.5 °C, 1.0 °C, and 1.5 °C. In addition, based on the depth distribution (5–20 m) of deposits in the Amney Machen rock-ice avalanche case (Paul, 2019; Zhang et al., 2019), the stress distribution inside the deposits is estimated to be 87.5–350 kPa. Here, the density of the rock-ice mixtures is estimated at 1750 kg/m^3. Therefore, the study selected the confining pressure of 200 kPa to reproduce the stress conditions for the deformation processes of the rock-ice deposits. Considering the rock-ice avalanche deposits are generally subjected to their gravity only, and combining with the subsidence characteristics of the rock-ice deposit dam of the Amney Machen case, the axial stress loading rate in this study was set to 1.2 mm/min. To investigate the mechanical properties of ice-rock mixtures under the situation that ice-meltwater cannot be drained in time, and the damage mechanism caused by meltwater, undrained triaxial tests were conducted in this study.

The framework of the test is as follows. First, we control the operating environment temperature of the laboratory with the help of natural temperature. The series of tests were performed in November–December 2023 in Beijing, China. This period was the winter season at the test site, and the sub-zero, low room temperature of the laboratory (0–2 °C) ensured the successful execution of the tests. In addition, before each triaxial test is performed, we control the temperature of silicone oil in the refrigeration system to keep it to about −5 °C, to avoid sample melting caused by too long-term temperature control for the pressure chamber. Finally, we cooled the pressure chamber in advance by pre-testing to ensure that the samples were directly placed in a low-temperature environment during the formal test. After the above preparations are completed, the formal procedure for temperature-controlled triaxial testing begins: (1) The prepared sample was removed from the freezer, the sample-making cylinder was removed, and the rubber membrane was installed. After securing the sample to the triaxial test platform and ensuring that the drain and vent channels are airtight, install the pressure chamber and begin filling the chamber with silicone oil at a low temperature. The total time for the process is about 10 min, but it requires a rich operating experience. (2) After the silicone oil is injected into the pressure chamber, the confining pressure is maintained at 200 kPa by the servo-controlled actuators and held for 30 min. During this process, the temperature of the silicone oil in the pressure chamber was controlled below 0 °C. (3) The temperature of the silicone oil in the pressure chamber is adjusted to the target temperature via the temperature control system. Then, the sample is left in the pressure chamber for a certain period (i.e., temperature control duration). (4) The axial load was applied by the axial loading system at a strain rate of 1.2 mm/min, and the test was terminated when the axial strain in the sample reached 20%.

(5) Ice meltwater can cause difficulties in disassembling samples for some conditions after the test is completed. For this reason, we refroze some samples through the temperature control system immediately after the test, which helped to complete the successful disassembly of the samples and the macroscopic damage characteristics study.

In this study, we focused on the influence of ice content, pressure chamber temperature, and temperature control duration (TCD) on the thermodynamic behavior of rock-ice mixtures. Here, TCD corresponds to the duration of the melting season in the actual scenario. Three groups of ice content, environment temperatures, and TCD were set for the tests. The confining pressure was controlled to be 200 kPa, and the axial loading rate was the same for all tests. Detailed test conditions of this study are shown in Table 4.

3. Results

3.1. Melting behaviors of rock-ice mixtures

3.1.1. Macro-deformation characteristics

During the melting test, the camera recorded the macroscopic toppling deformation characteristics of the samples at different moments. Fig. 5 demonstrates the melting process of rock-ice mixture samples with I_c of 0.75, 0.50, and 0.25 in a temperature environment of 1 °C. The ice melting in this section is mainly caused by the heat transfer between samples and the boundary field (Pudasaini, 2024). Compared to the other two samples, the sample with an I_c of 0.75 produced more ice meltwater after 10 min, which gathered at the bottom and flowed into the tray, as indicated by the black arrow in Fig. 5a. Meanwhile, the sample with I_c of 0.75 also suffered a visible toppling deformation during the following process, and the overall collapse occurred after 60 min (see Fig. 5f). In contrast, samples with I_c of 0.50 and 0.25 produced less ice meltwater and could not be directly observed. Although the samples with I_c of 0.50 and 0.25 also produced inclinations within 60 min, the inclinations were not severe enough to cause the sample to collapse.

To further investigate the meltwater aggregation mode and the basal deformation characteristics of the samples, we investigate the bottoms of different samples after 60 min. Fig. 6a–c provides a detail of the basal damage surface of the three sets of samples in the 1 °C environment. It should be noted that after 60 min, we manually lifted the samples from the top of them, and all three sets of sample bodies were smoothly separated from their basal damage areas. The results of observations showed that the sample with an I_c of 0.75 produced more meltwater (Fig. 6a), and the basal damage zone's thickness was larger than the other two samples (Fig. 6b–c). Nevertheless, some meltwater was also collected at the bottom of the samples with I_c of 0.50 and 0.25, and the meltwater of the sample with I_c of 0.50 was more than that of the sample with I_c of 0.25. Among the three samples, the bottom damage zone of the sample with an I_c of 0.25 maintains a better original cylindrical shape. Fig. 6d–f illustrates the final melting characteristics of three samples with different I_c in a 0.5 °C environment. Visible, the bottom of the sample with I_c of 0.75 gathered some meltwater, which was distributed in a circular form around the sample but did not develop a flow behavior. After 60 min in a 0.5 °C environment, none of the three samples collapsed, although they developed different deformations.

Table 4
Temperature-controlled triaxial test conditions.

Test ID	Sample ID	I_c	T (°C)	C_p (kPa)	TCD (min)
1–3	RIM 01-03	0.25	0.5	200	20/40/60
4–6	RIM 04-06	0.25	1.0	200	20/40/60
7–9	RIM 07-09	0.25	1.5	200	20/40/60
10–12	RIM 10-12	0.50	0.5	200	20/40/60
13–15	RIM 13-15	0.50	1.0	200	20/40/60
16–18	RIM 16-18	0.50	1.5	200	20/40/60
19–21	RIM 19-21	0.75	0.5	200	20/40/60
22–24	RIM 22-24	0.75	1.0	200	20/40/60
25–27	RIM 25-27	0.75	1.5	200	20/40/60

Notes: T indicates pressure chamber's temperature and C_p means the confining pressure.

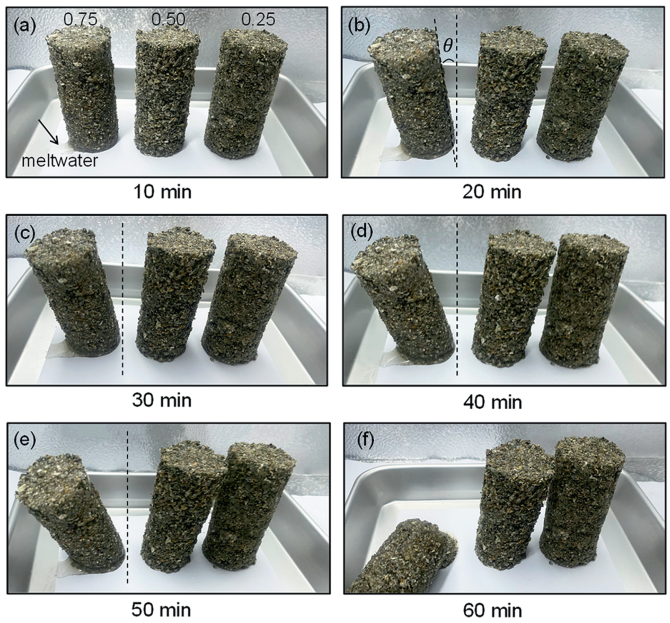

Fig. 5. Melting test results of samples with different ice contents (0.75, 0.5, 0.25) under a temperature of 1 °C: (a–f) deformation characteristics of the samples at different moments. The black dashed line in the figure is the baseline for calculating the inclination. Here, min means minutes.

We used the inclination degree to characterize the degree of sample deformation in the melting test. The specific calculation approach is as follows. The angle at which the sample is deflected from the plumb line is defined as the dip angle (θ) of the sample (see Fig. 5b), and it is assumed that the maximum inclination of the sample is 90°, i.e., the sample collapses. The inclination degree is the ratio of the sample dip angle (θ) to 90°. Fig. 7a presents the characteristics of inclination degree variation during melting of six samples in different temperature environments. The results indicate that environmental temperature and I_c can promote the deformation of the rock-ice mixture samples. The test condition with the greatest inclination was an I_c of 0.75 and an environment temperature of 1.0 °C. Under this test condition, the inclination degree of the sample reached 0.44 at 50 min, which exceeded all other samples. The samples with I_c of 0.25 and 0.50 in the 0.5 °C environment were the least deformed, with an inclination degree of 0.07 and 0.13 at 60 min, respectively. Further, the volume of basal gathered meltwater of different samples was counted using the absorbent paper. As shown in Fig. 7b, the samples with an I_c of 0.75 produced more meltwater in the melting test (0.36 mL and 0.82 mL), compared to the samples with a low ice content (0, 0.12, and 0.25 mL). Overall, meltwater statistics point to the critical control of ambient temperature and ice-component fractions on the ablation state of the mixture.

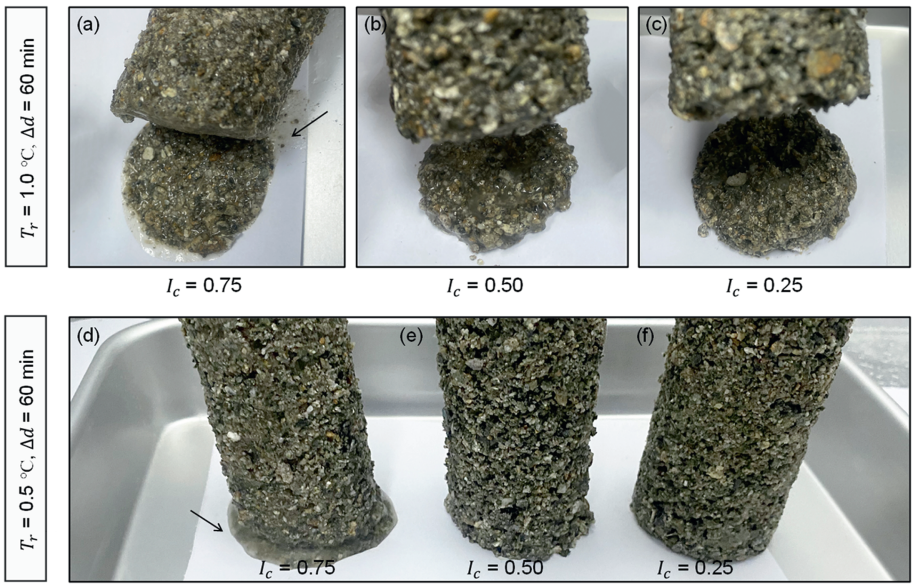

Fig. 6. Basal damage characteristics of the samples: (a–c) the deformation characteristics of the samples in the 1.0 °C environment; and (d–e) results of the samples in the 0.5 °C environment. Here, T_r means the temperature of the test zone and Δd Means the duration of the test.

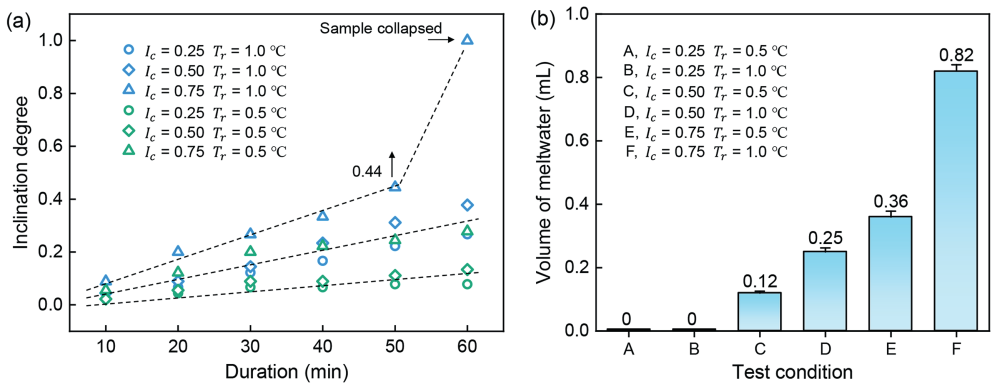

Fig. 7. Deformation and melting characteristics of the samples: (a) Inclination degree of different samples in the melting test, and (b) Volume of the basal gathered meltwater.

3.1.2. Damage mechanism analysis

Based on melting test results, meltwater seepage patterns and deformation characteristics of rock-ice mixtures are summarized. Firstly, observations from the tests suggest that only the ice debris in the surface layer of the sample undergoes melting for 60 min, which is due to the surface layer being the main temperature exchange boundary (Fig. 8a). In addition, the melting of ice debris leads to an increase in its roundness and weakens the local cohesion strength of the rock-ice mixture (Fig. 8b–c). In this series of melting tests, the sample's surface layer's melting depth was about 0.2–0.6 cm. As shown in Fig. 8a, the ice meltwater from the surface layer percolated vertically downward and collected at the bottom of the sample. The bottom of the sample is in a state of water-rock debris mixing due to the meltwater gathered in the region, resulting in mixtures with almost zero cementation strength. The basal mixtures with low shear strength could not withstand the gravity of the overlying mass, leading to the rapid formation of the basal failure zone (Fig. 8d). In addition, we believe the basal meltwater made the cohesion and occlusion between the rock particles almost disappear entirely, as shown in Fig. 8e. Investigations at the deposits of the Amney Machen rock-ice avalanche revealed a similar phenomenon, as shown in Fig. 8f, where the ice meltwater infiltrated along the internal pores of the mixture. When clay or mudstone debris material is present within the mixture, meltwater mixing with it will result in localized mudflows. In the field, meltwater convergence was also observed at the base of the rock-ice deposits dam (Fig. 8g), consistent with the meltwater migration pattern revealed by the melting tests.

3.2. Results of temperature-controlled triaxial test

3.2.1. Macro-damage and stress-strain characteristics

Based on the test results, we sequentially analyze the influence of TCD, environment temperature, and ice content on rock-ice mixtures' stress-strain characteristics and damage modes. Fig. 9a illustrates the stress-strain curve for samples with I_c of 0.75 and in a 1.0 °C environment. In this set of tests, we only change the TCD before loading. The results show that the peak deviator stress of the samples decreases with the increase of the TCD. The values of peak deviator stress corresponding to the TCDs, 20 min, 40 min, and 60 min, are 230.38 kPa, 183.82 kPa, and 102.87 kPa, respectively. In addition, the stress-strain curves of the three samples showed almost no stress increase during the initial deformation stage, as shown in region A in Fig. 9a. We suggest that the

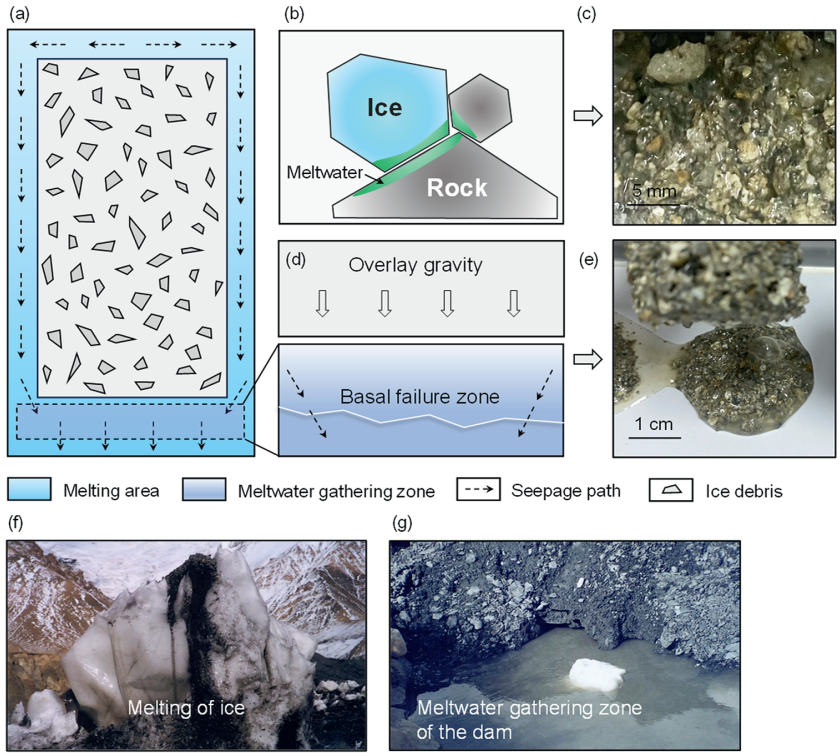

Fig. 8. Melting-induced deformation mechanism of the rock-ice mixtures: (a) melting pattern of the rock-ice mixtures, (b–c) meltwater generated inside the rock-ice mixtures, (d–e) basal damage of the samples caused by the meltwater gathering, (f) ice melting phenomenon in the field, and (g) meltwater gathered at the bottom of the rock-ice deposits dam.

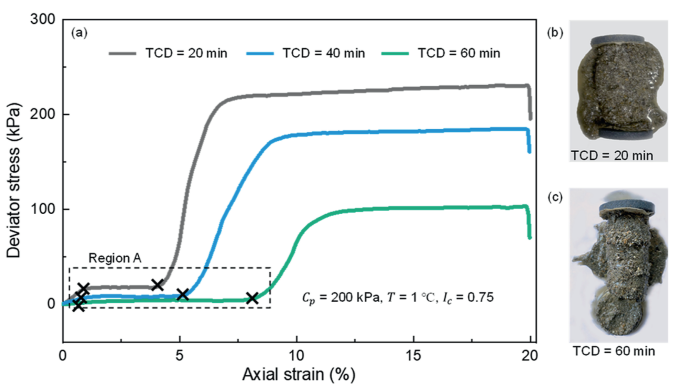

Fig. 9. Test results at different TCD conditions: (a) stress-strain characteristics of the samples with different control duration conditions; and (b–c) macro-damage characteristics of the samples. Here, TCD means the temperature control duration and C_p means the confining pressure.

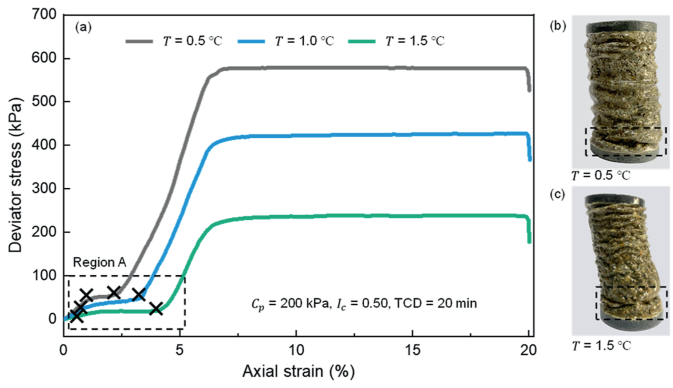

Fig. 10. Test results at different temperature conditions: (a) stress-strain results of the samples with different temperature conditions; and (b–c) macro-deformation characteristics of the samples. The samples shown in this graph are not samples from when the test was just completed but frozen by the temperature control system.

meltwater gathering zone at the sample bottom led to this result. As analyzed in Section 3.1.2, the mixture in the basal failure zone loses its resistance to shear and compress, which leads to a weak pre-stress change in the stress-strain curve.

In this study, we term the process of weak stress change in the pre-stress-strain curve as the basal strain stage. Further, the basal strain value of a sample is determined by the initial axial strain, demonstrated by the strain between two cross symbols in Fig. 9a. Based on this, we found that the basal strain stage exhibits different scales for different TCDs. The values of basal strain corresponding to the TCDs, 20 min, 40 min, and 60 min, are 4.07%, 5.13%, and 8.25%, respectively. The increase in TCD leads to a rise in the amount of meltwater, which in turn leads to an expansion of the basal failure zone, finally showing up as an increase in the basal strain. Fig. 9b–c illustrates the damage characteristics of the samples with TCDs of 20 min and 60 min. Compared with samples in Fig. 9b, the melting state of the sample in Fig. 9c is more serious, as evidenced by the melting depth of the surface layer (0.35 cm of Fig. 9b versus 0.65 cm of Fig. 9c) and the volume of the basal damage zone. It should be noted that meltwater was challenging to control during sample disassembly, and we removed some of the splashed or spilled meltwater.

The stress-strain results and damage characteristics of the samples under three different temperature environments (0.5 °C, 1 °C, and 1.5 °C) are shown in Fig. 10. In this set of tests, the I_c of the samples all set as 0.50, and the TCD all set as 20 min. To better

observe the deformation characteristics of the samples and the meltwater gathering pattern, we refroze the samples after the tests were completed. Fig. 10b–c illustrates the samples after refreezing, with a clear damage region appearing at the sample bottom with visible compression and folding zone, as indicated by the black dashed boxes. Meanwhile, the surface layer of the sample in the 1.5 °C environment collected more meltwater (see Fig. 10c), which appears as ice formed by refreezing, compared to the sample in the 0.5 °C environment (Fig. 11b). The stress-strain results demonstrated in Fig. 11a indicate that the peak deviator stress of the samples continues to decrease as the temperature increases. In this set of tests, the samples also showed an initial basal strain stage, and the temperature increase exacerbated the basal strain effect (see the black dashed box in Fig. 11a).

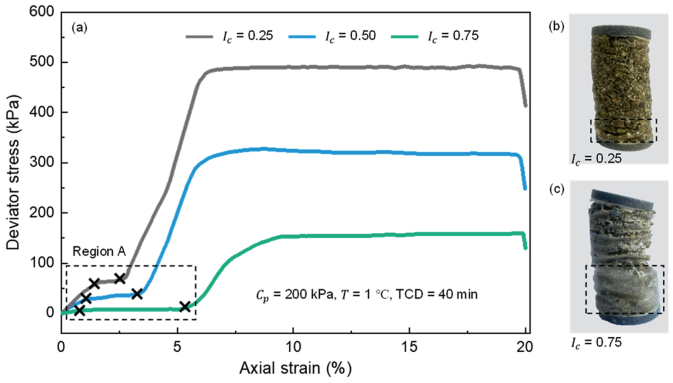

Fig. 11. Test results at different ice content conditions: (a) stress-strain characteristics of the samples with different ice contents, and (b–c) macro-deformation characteristics of the samples.

The test results for samples with different ice contents showed that the strength of the samples in the thawing environment decreased with increasing ice content, keeping other variables consistent (environment temperature is 1.0 °C and TCD is 40 min). Specifically, the values of peak deviator stress corresponding to the I_c, 0.25, 0.50, and 0.75, are 489.14 kPa, 327.13 kPa, and 158.76 kPa, respectively. Similarly, an increase in ice content exacerbates the basal strain behavior of the sample (see region A in Fig. 11a). Fig. 11b–c demonstrates the deformation characteristics of two samples with I_c of 0.25 and 0.75 after the tests. The sample with an I_c of 0.75 collected more meltwater at the bottom (Fig. 11c), compared to the sample with an I_c of 0.25 (Fig. 11b). Nevertheless, the bottom of the sample with an I_c of 0.25 also gathered a small amount of meltwater and formed a visible compression folding zone (see the black dashed box in Fig. 11b).

3.2.2. Failure mode analysis

The stress-strain results of all triaxial tests in this study are presented in Fig. 12. The horizontal and vertical axes in Fig. 12 indicate different I_c and environment temperature sets, respectively. The results of the relevant series of tests are plotted in different sub-stress-strain diagrams. Based on the characteristics of the stress-strain curves from 27 sets of tests, we classify the deformation processes of rock-ice mixture samples in thaw environments (Temperature >0 °C) into the basal strain stage and the general deformation stage (Fig. 13). As analyzed in Section 3.2.1, meltwater from the surface layer of the rock-ice mixture gathered at the bottom region through the surface seepage path, formed a meltwater basal gathering zone (see stage A in Fig. 13). The weak strength characteristics of the basal zone lead to an easily initial compression process, even without additional principal stresses. As a result, the stress-strain curve in the basal strain stage is very flat until the basal zone is compacted (see stage B in Fig. 13).

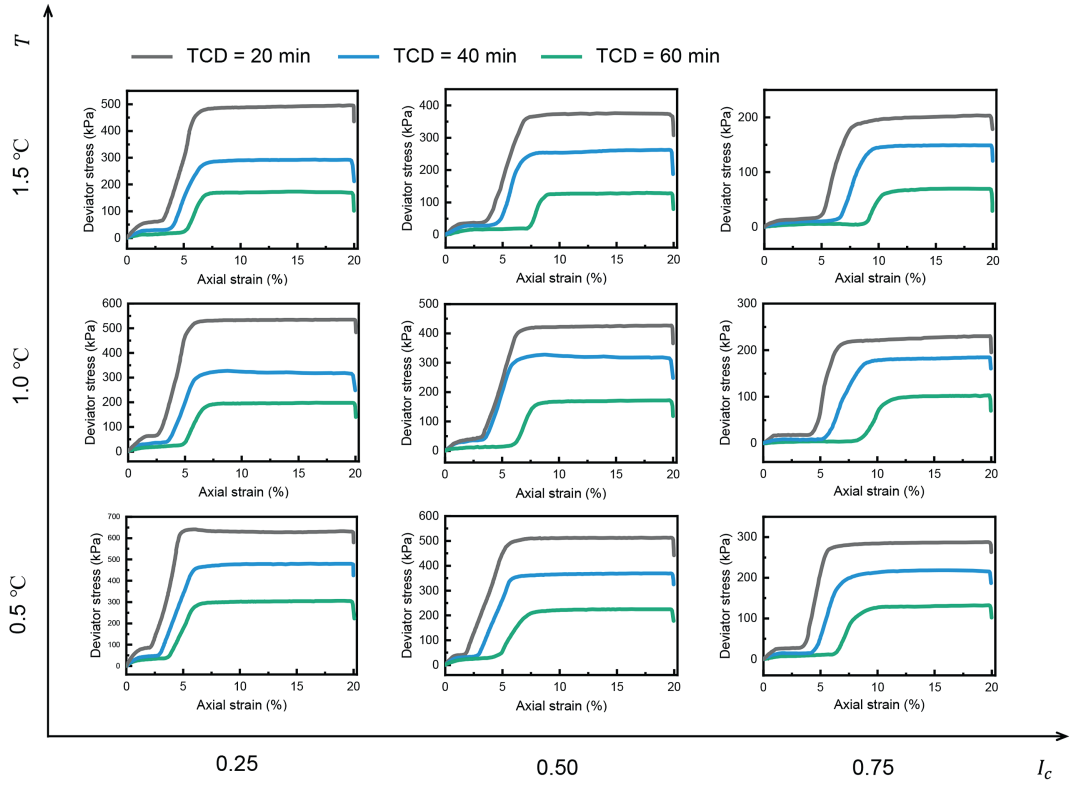

Fig. 12. Stress-strain results of all the temperature-controlled triaxial tests.

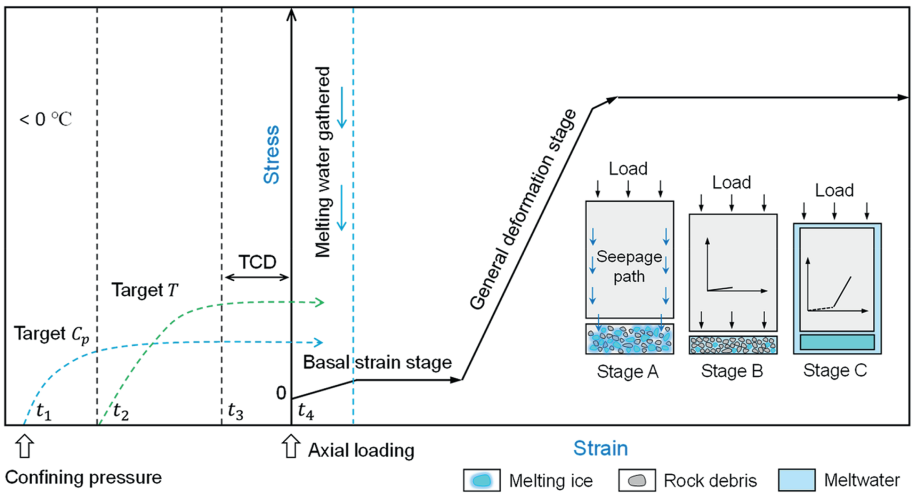

Fig. 13. The stress-strain mechanism of the rock-ice mixtures sample in thaw environment.

Nevertheless, the degree of ice debris melting and rock debris content within the basal failure zone will have an impact on the basal compaction process. Subsequently, the unmelted portion of the rock-ice mixture sample begins regular compressive deformation with a rapid increase in stress and strain (see stage C in Fig. 13). Note that the confining pressure control (t_1) and pressure chamber temperature control (t_2) were completed before axial loading (t_4) for all triaxial tests. The temperature adjustment process ($t_2 - t_3$, about 10–15 min) also provides room for the formation of basal meltwater zones. In summary, the damaged base of the sample caused by meltwater is the dominant contributor to basal strain effects.

3.3. Joint effects of multi-factors on thermodynamic behavior

Based on the results of 27 groups of temperature-controlled triaxial tests, we analyzed the mechanism of the joint effect of I_c, environment temperature, and TCD on the thermodynamic properties of rock-ice mixtures. This study focuses on analyzing the peak deviator stresses and basal strains of rock-ice mixtures. Fig. 14 illustrates the peak deviator stress results for samples from 27 sets of tests, where we have divided the data into three sections based on the environment temperature. Previous analyses have suggested that an increase in both the TCD and the ice content can decrease the peak strength of the rock-ice mixtures. However, in this section's peak deviator stress distribution plots, we find that a TCD of 60 min and an I_c of 0.75 are the key controlling conditions for the decrease in sample strength. Specifically, the value 40% away from the lower limit of the peak stress distribution range in each section is set as the cutoff point, as the triangles are shown in Fig. 14a–c. Based on this, we found that individuals with peak deviator stress less than 40% of the maximum value in each section were those samples with I_c of 0.75 or TCD of 60 min indicated by the black dashed line in Fig. 14a–c. When the I_c of the sample was 0.75, and the TCD of the test was 60 min, the sample showed a remarkably low peak deviator stress, with values of 128.12 kPa, 100.44 kPa, and 70.24 kPa for three sections, respectively. Fig. 14d illustrates the point distribution of peak deviator stress for 27 groups of tests, with environment temperature as the axis of variation. Overall, the range of peak deviator stress distributions and median values are smaller for the samples in higher temperature environments, which characterizes the role of temperature increase in controlling the thermodynamic properties of rock-ice mixtures under different scenarios.

The statistical results of the basal strain of 27 samples show that the growth of both TCD and I_c leads to an increase in the basal strain (Fig. 15a–c). Compared to the peak deviator stress, we found that more stringent conditions are required for high basal strains (greater than 40% maximum value). Large base strains occur only when I_c is 0.75, or I_c is greater than 0.50, and TCD is 60 min, indicated by the region with a black dashed line in Fig. 15a–c. The extent of basal strain is related to the amount of meltwater in the basal damage zone and depends on the content of rock debris within that zone. When the conditions of I_c being 0.75 and TCD being 60 min are satisfied jointly, the basal strain values of the samples in the environments 0.5 °C, 1.0 °C, 1.5 °C are 6.18%, 8.36%, and 8.62%, respectively. The results of point distribution of basal strains of all samples show that the median values of basal strains of different groups increase with increasing temperature, and the range of basal strains widens (Fig. 15d), indicating the overall influence of environment temperature on the basal damage of rock-ice mixtures. In addition, we counted the mass loss of different post-test samples, which indicates the material lost from the surface layer and the substrate of the sample due to ice melting. The mass loss ratio is defined as the ratio of mass lost to the initial mass of the sample. The results showed a higher mass loss ratio of the samples under conditions of high I_c and high TCD. The mass loss ratio reached its maximum value (28.69%) when the sample with an I_c of 0.75 was left in an environment of 1.5 °C for 60 min. Similarly, we find that the mass loss exhibits a positive feedback on I_c with TCD (Fig. 16a–c), and is dominantly controlled by the ambient temperature (Fig. 16d).

4. Discussion

4.1. Secondary disasters from rock-ice avalanche deposits

According to the study of the thermodynamic behavior of rock-ice mixtures in thaw environments, this section aims to discuss the secondary disasters from the rock-ice deposits caused by increased temperature. Related studies have frequently reported the occurrence of secondary slides on historic deposits of landslides and rock avalanches, raising people's awareness of the potential risks of old deposits (Suwa et al., 2010; Klimeš et al., 2016). However, developing secondary hazards for rock-ice avalanche deposits formed by glacier detachment in the region of alpine glaciers also

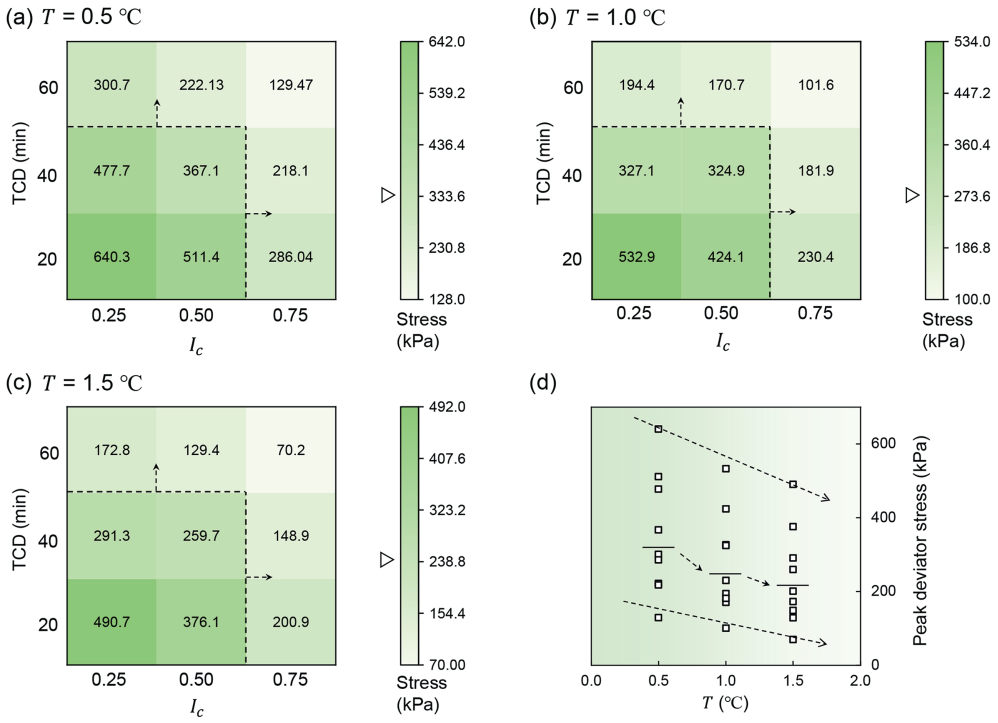

Fig. 14. The variation characteristics of the peak deviator stress of the different tests: (a–c) results of the different temperature conditions; and (d) influence of the environment temperature on the peak deviator stress. The short black line indicates the median value.

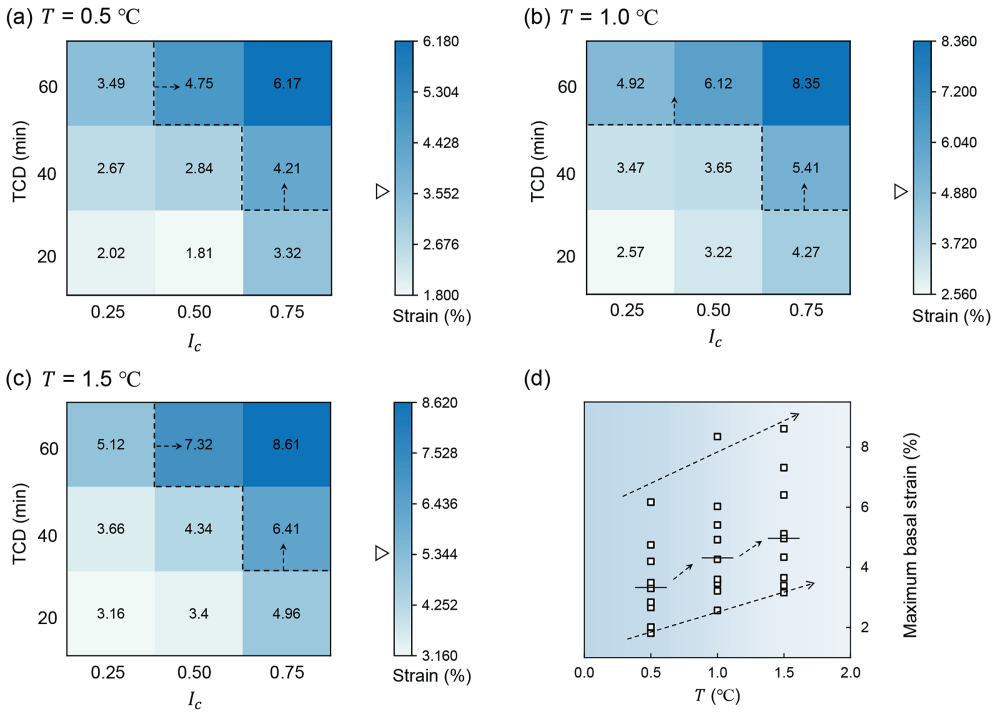

Fig. 15. The variation characteristics of the maximum basal strain of the different tests: (a–c) results of the different temperature conditions; and (d) influence of the environment temperature on the basal strain. The short black line indicates the median value.

needs more attention. Borgatti et al. (2006) proposed that secondary sliding of old deposits requires certain external conditions, such as rainfall, fluctuations in the water table, and favorable topography. According to Zou et al. (2023), in the Amney Machen case, deposits accumulated in the entrainment area with a volume greater than 2.5×10^6 m^3 and an average thickness of about 5 m. At the same time, the average slope of the entrainment area exceeds 10° and reaches 15°–20° in localized areas. As shown in Fig. 17a, when the environment temperature rises, meltwater from melting surface ice debris in rock-ice avalanche deposits is transported

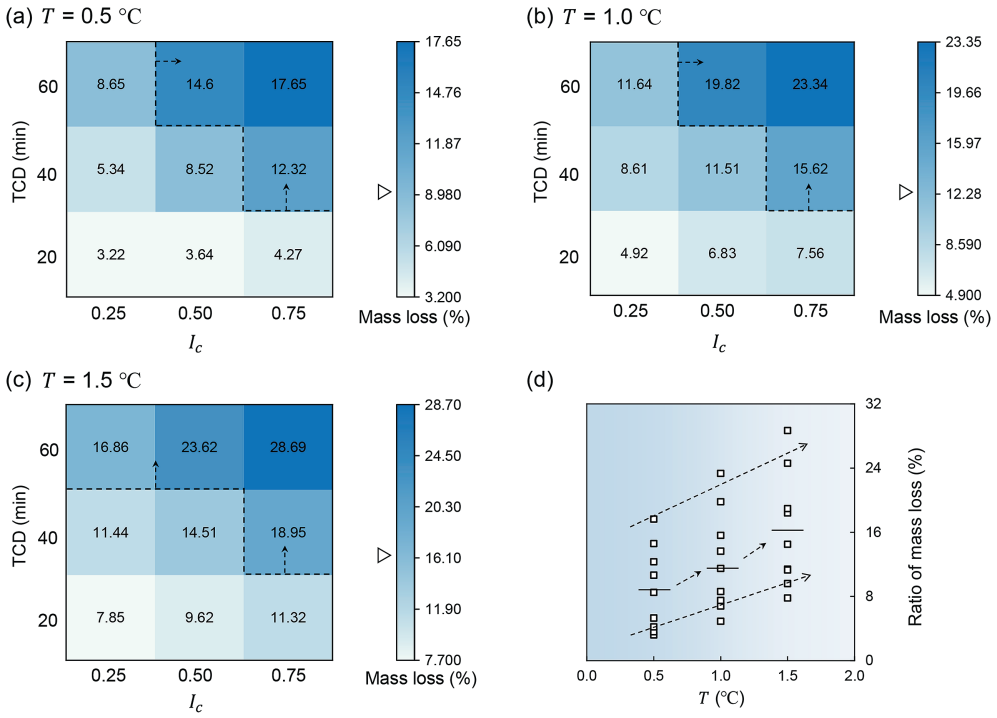

Fig. 16. The ratio of mass loss for the samples: (a–c) results of the different temperature conditions; and (d) influence of the environment temperature on the mass loss of rock-ice mixtures.

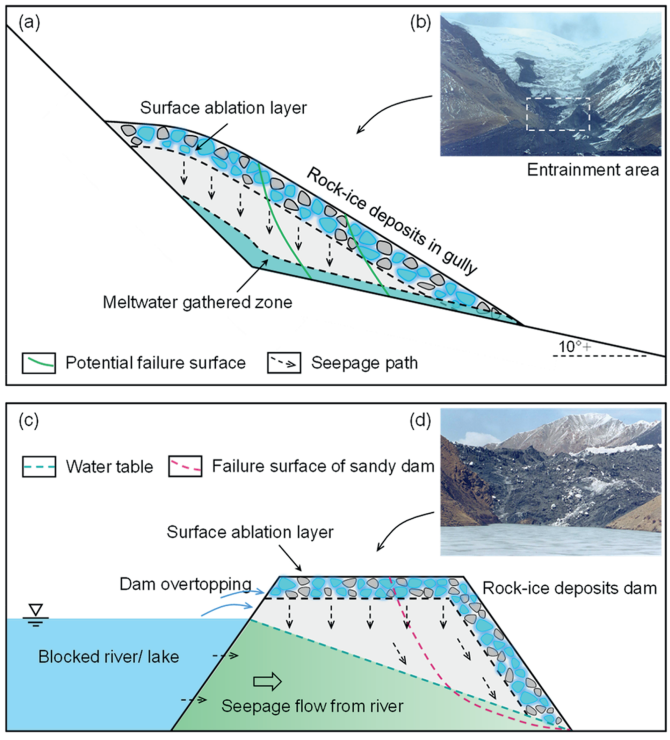

Fig. 17. Potential disasters from the rock-ice deposits: (a–b) secondary sliding disaster from the rock-ice deposits accumulated at the entrainment area; and (c–d) the potential deformation and failure of the rock-ice deposits dam caused by the ice melting behavior.

downward along the internal seepage channels. According to the field results, the surface melting depth of the 2004 Amney Machen rock-ice avalanche deposits can be up to 1.1 m. Seepage of ice meltwater can form a meltwater gathering zone at the bottom of the deposits, leading to a sharp reduction in deposits' shear strength, which in turn evolves into a potential sliding zone and causes a retrogressive failure behavior, indicated by the red lines in Fig. 17a. The mechanism of basal sliding zones of landslides caused by rainfall or groundwater has been reported by many studies (Tsaparas et al., 2002; Collins and Znidarcic, 2004; Piciullo et al., 2018). Therefore, we suggest that when the amount of ice meltwater reaches a certain threshold under favorable topographic conditions, the rock-ice avalanche deposits are prone to secondary sliding, resulting in a new disaster. In this scenario, the basal sliding zone of rock-ice deposits is similar to the basal failure zone of the samples in this study. For further dynamic analysis, the secondary rock-ice mass flow and catastrophic propagation of rock-ice deposits can be simulated by utilizing the seminal, physics-based, multi-phase, thermo-mechanical rock-ice avalanche model (Pudasaini, 2024) and the exact, analytical solutions therein.

Dams formed by rock-ice deposits are also a critical source of potential hazards (Fig. 17c). Different from the failure processes of the sand and gravel dam model (Zhong et al., 2019; Bui and Nguyen, 2021), the melting of ice debris inside the rock-ice avalanche deposits can create a new series of issues. For example, ice debris meltwater can lead to the formation of large numbers of subsidence cracks, collapse holes, cavities, and water migration channels within the dam body, which can affect the structural stability of the dam. On the other hand, as the global climate warms, the flow into the lake formed by melting water from snow and ice will increase, causing the lake level to rise sharply (Zhang et al., 2011; Song et al., 2014). Rising lake levels will accelerate the melting of ice debris, further accelerating the dam's failure. Given that in the case of the 2004 Amney Machen rock-ice avalanche, the ice content in the dam body was as high as 70%–80%. When the lake level rises close to the dam top, the

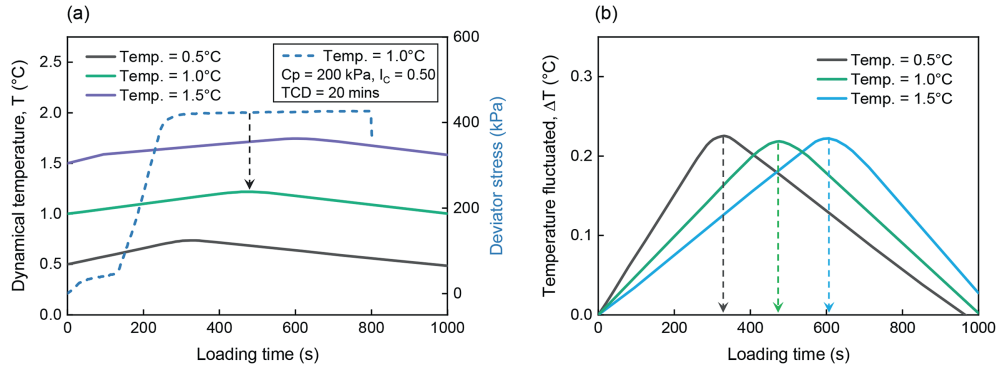

Fig. 18. Potential disasters from the rock-ice deposits: (a) Changing of the peripressure fluid temperature during the loading process, and (b) Temperature anomalous behavior of the peripressure fluid under different conditions.

buoyant force of the pore pressure on the ice debris increases, which in turn accelerates the subsidence and breakup of the surface layer of the dam (Fig. 17d). Besides, lake water seepage can accelerate the connectivity of ice meltwater seepage channels within the dam, leading to widespread dam collapse and large-scale flooding hazards (Delaney and Evans, 2015; Wu et al., 2020; Liu et al., 2021). If the melting of ice debris results in an excessive drop in the dam height, it can lead to the overtopping of the lake (Tingsanchali and Chinnarasri, 2001; Kuo et al., 2007) and accelerate the overall collapse of the dam. As a result, rising temperatures will pose a significant risk to the stability of rock-ice mixture dams, which in turn leads to severe flooding (Pudasaini and Mergili, 2019; Shugar et al., 2021).

4.2. Potential control factors

Relevant studies have shown that the arrangement of particles with different grain sizes affects mixtures' shear mode and stress-strain characteristics (Xiao et al., 2014; Alhani et al., 2020; Wu et al., 2023). As the site deposits of the Amney Machen rock-ice avalanche (Fig. 1a–c), the ice debris' size distribution is wide-ranging and poorly homogenized. In contrast, the size distribution of mudstone and chert clasts within the deposits is relatively uniform. However, the components of the deposits can vary from different rock-ice avalanche cases. Therefore, we considered only ice content, environment temperature, and temperature control duration as three key factors in this work. Also, the variation of the confining pressure is important for the study of the mechanical properties of the material. As Chen et al. (2022) stated, the high confining pressure environment contributes to the increased bonding of the ice material within the permafrost in a frozen environment, which can affect the volumetric deformation of the ice-rock mixture.

In addition, we found that even though the temperature control system attempted to maintain the temperature of the peripressurized fluid at a pre-set value, there was still some variation in the monitored temperature. Fig. 18a provides temperature monitoring data of the peripressure fluid during the shearing of a sample with an ice content of 0.50 at different target temperatures. The results show that the fluid temperature decreases after a slight increase. Eliminating the insulation failure in the triaxial pressure chamber, we suggest that the heat exchange due to the melting of ice particles during shear affected the temperature of the peripressure fluid. When the rapid melting process in the surface and basal zones of the sample is finished (see arrow in Fig. 18a), the fluid temperature begins to converge to the target temperature. The results of the floating temperature difference show that the temperature anomalous behavior of the peripressure fluid ends sooner at lower ambient temperatures (Fig. 18b), indicating a weak ablation state of the sample. Thus, heat migration due to the ice-melting behavior can affect the mechanical strength of rock-ice mixtures and also alter the surrounding energy field.

5. Conclusions

Combined with the field investigation results of rock-ice mixtures in the accumulation area of the historical rock-ice avalanche, the melting pattern and thermodynamic behavior of the rock-ice mixtures were investigated through the melting and temperature-controlled tests. The melting test results indicate that the melting region of the rock-ice mixture was mainly located in the surface layer of the sample. When the ice debris in the surface layer is melted, the meltwater will be transported downward along the surface seepage path, eventually forming a meltwater gathered zone at the bottom of the sample. The formation of the meltwater gathered zone leads to a sharp decrease in the compression and shear strength of the basal zone, where the cohesion and occlusion between the rock debris almost disappear entirely. The triaxial tests show that the basal damaged zone due to meltwater gathering can lead to a basal strain effect during the initial compression process. We found that the low strength of the basal zone leads to a rapid compressive deformation with little need for additional axial stresses at this stage. Meanwhile, the results of 27 sets of triaxial tests indicate that increases in ice content, environment temperature, and temperature control duration all lead to a decrease in the peak deviator stress of rock-ice mixtures and a promotion of the basal strain effect and mass loss. We suggest that in the background of global climate warming, the melting of ice debris within large rock-ice avalanche deposits is highly likely to lead to secondary hazards, such as the re-sliding of deposits in gullies and flooding triggered by the failure of rock-ice mixture deposit dams. Therefore, these risky mixed ice-rock deposits should be monitored, such as for their deformation and meltwater seepage characteristics.

CRediT authorship contribution statement

Wenbin Chang: Writing – original draft, Investigation, Methodology, Validation. **Aiguo Xing:** Writing – review & editing, Funding acquisition, Supervision. **Changbao Guo:** Supervision, Writing – review & editing. **Wenbo Zhao:** Methodology, Visualization.

Declaration of competing interest

The authors declare that they have no known competing financial interests or personal relationships that could have appeared to influence the work reported in this paper.

Acknowledgements

This study was supported by the National Key R&D Program of China (Grant Nos. 2023YFC3008300 and 2023YFC3008302).

References

Akagawa, S., Nishisato, K., 2009. Tensile strength of frozen soil in the temperature range of the frozen fringe. Cold Reg. Sci. Tech. 57 (1), 13–22.
Alhani, I.J., Noor, M.J.B.M., Al-Bared, M.A.M., Harahap, I.S.H., Albadri, W.M., 2020. Mechanical response of saturated and unsaturated gravels of different sizes in drained triaxial testing. Acta Geotech. 15, 3075–3093.
An, B., Wang, W., Yang, W., Wu, G., Guo, Y., Zhu, H., et al., 2022. Process, mechanisms, and early warning of glacier collapse-induced river blocking disasters in the Yarlung Tsangpo Grand Canyon, southeastern Tibetan Plateau. Sci. Total Environ. 816, 151652.
Arenson, L.U., Johansen, M.M., Springman, S.M., 2004. Effects of volumetric ice content and strain rate on shear strength under triaxial conditions for frozen soil samples. Permafrost. Periglac. 15 (3), 261–271.
Barla, G., Barla, M., Debernardi, D., 2010. New triaxial apparatus for rocks. Rock Mech. Rock. Eng 43, 225–230.
Borgatti, L., Corsini, A., Barbieri, M., Sartini, G., Truffelli, G., Caputo, G., Puglisi, C., 2006. Large reactivated landslides in weak rock masses: a case study from the Northern Apennines (Italy). Landslides 3, 115–124.
Bui, H.H., Nguyen, G.D., 2021. Smoothed particle hydrodynamics (SPH) and its applications in geomechanics: from solid fracture to granular Behaviour and multiphase flows in porous media. Comput. Geotech. 138, 104315.
Chang, W.B., Xing, A.G., 2025a. Warming-driven weakening of basal ice layer as a critical cause of ice avalanche activation. Cold Reg. Sci. Tech. 236, 104513.
Chang, W.B., Xing, A.G., 2025b. Influence of ice particles melting on the propagation of rock-ice avalanches: experimental investigation. Landslides 22 (6), 2073–2088.
Chen, S., Ma, W., Li, G., 2022. A novel approach for characterizing frozen soil damage based on mesostructure. Int. J. Damage Mech. 31 (3), 444–463.
Collins, B.D., Znidarcic, D., 2004. Stability analyses of rainfall induced landslides. J. Geotech. Geoenviron. Eng. 130 (4), 362–372.
Delaney, K.B., Evans, S.G., 2015. The 2000 Yigong landslide (Tibetan Plateau), rockslide-dammed lake and outburst flood: review, remote sensing analysis, and process modelling. Geomorphology 246, 377–393.
Deline, P., Gruber, S., Amann, F., Bodin, X., Delaloye, R., Failletaz, J., et al., 2021. Ice loss from glaciers and permafrost and related slope instability in high-mountain regions. In: Haeberli, W., Whiteman, C. (Eds.), Snow and ice-related Hazards, Risks, and Disasters. Elsevier, Netherlands, pp. 501–540. AMS.
Falaschi, D., Kääb, A., Paul, F., Tadono, T., Rivera, J.A., Lenzano, L.E., 2019. Brief communication: collapse of 4 Mm 3 of ice from a cirque glacier in the Central Andes of Argentina. Cryosphere 13 (3), 997–1004.
Faillettaz, J., Sornette, D., Funk, M., 2011. Numerical modeling of a gravity-driven instability of a cold hanging glacier: reanalysis of the 1895 break-off of Altelsgletscher, Switzerland. J. Glaciol. 57 (205), 817–831.
Faillettaz, J., Funk, M., Vincent, C., 2015. Avalanching glacier instabilities: review on processes and early warning perspectives. Rev. Geophys. 53 (2), 203–224.
Fan, X., Dufresne, A., Whiteley, J., Yunus, A.P., Subramanian, S.S., Okeke, C.A., et al., 2021. Recent technological and methodological advances for the investigation of landslide dams. Earth Sci. Rev. 218, 103646.
Fan, X., Yunus, A.P., Yang, Y.H., Subramanian, S.S., Zou, C., Dai, L., et al., 2022. Imminent threat of rock-ice avalanches in High Mountain Asia. Sci. Total Environ. 836, 155380.
Fischer, L., Huggel, C., Kääb, A., Haeberli, W., 2013. Slope failures and erosion rates on a glacierized high-mountain face under climatic changes. Earth Surf. Proc Land 38 (8), 836–846.
Fitzsimons, S.J., McManus, K.J., Sirota, P., Lorrain, R.D., 2001. Direct shear tests of materials from a cold glacier: implications for landform development. Quat. Int. 86 (1), 129–137.
Gao, H., Yin, Y., Li, B., Gao, Y., Zhang, T., Liu, X., Wan, J., 2023. Geomorphic evolution of the Sedongpu Basin after catastrophic ice and rock avalanches triggered by the 2017 Ms6. 9 Milin earthquake in the Yarlung Zangbo River area, China. Landslides 20 (11), 2327–2341.
Gnyawali, K.R., Xing, A., Zhuang, Y., 2020. Dynamic analysis of the multi-staged ice–rock debris avalanche in the Langtang valley triggered by the 2015 Gorkha earthquake, Nepal. Eng. Geol. 265, 105440.
Huang, D., Meng, Q., Song, Y., Gu, D., Cen, D., Zhong, Z., 2023. Experimental study on the shear mechanical behavior of ice-rich debris–rock interface: effects of temperature, stress and ice content. Can. Geotech. J. 61 (6), 1051–1072.
Huggel, C., Zgraggen-Oswald, S., Haeberli, W., Kääb, A., Polkvoj, A., Galushkin, I., Evans, S.G., 2005. The 2002 rock/ice avalanche at Kolka/Karmadon, Russian Caucasus: assessment of extraordinary avalanche formation and mobility, and application of QuickBird satellite imagery. Nat. Hazards Earth Syst. Sci. 5 (2), 173–187.
Jacquemart, M., Loso, M., Leopold, M., Welty, E., Berthier, E., Hansen, J.S., et al., 2020. What drives large-scale glacier detachments? Insights from flat Creek glacier, St. Elias Mountains, Alaska. Geology 48 (7), 703–707.
Kang, C., Chan, D., Su, F., Cui, P., 2017. Runout and entrainment analysis of an extremely large rock avalanche—a case study of Yigong, Tibet, China. Landslides 14, 123–139.
Kääb, A., Leinss, S., Gilbert, A., Bühler, Y., Gascoin, S., Evans, S.G., et al., 2018. Massive collapse of two glaciers in western Tibet in 2016 after surge-like instability. Nat. Geosci. 11 (2), 114–120.
Kääb, A., Jacquemart, M., Gilbert, A., Leinss, S., Girod, L., Huggel, C., et al., 2021. Sudden large-volume detachments of low-angle mountain glaciers–more frequent than thought? Cryosphere 15 (4), 1751–1785.
Kermani, M., Farzaneh, M., Gagnon, R., 2007. Compressive strength of atmospheric ice. Cold Reg. Sci. Tech. 49 (3), 195–205.
Klimeš, J., Yepes, J., Becerril, L., Kusák, M., Galindo, I., Blahut, J., 2016. Development and recent activity of the San Andres landslide on el Hierro, Canary Islands, Spain. Geomorphology 261, 119–131.
Krautblatter, M., Funk, D., Günzel, F.K., 2013. Why permafrost rocks become unstable: a rock–ice-mechanical model in time and space. Earth Surf. Proc Land 38 (8), 876–887.
Kropáček, J., Vilímek, V., Mehrishi, P., 2021. A preliminary assessment of the Chamoli rock and ice avalanche in the Indian Himalayas by remote sensing. Landslides 18, 3489–3497.
Kuo, J.T., Yen, B.C., Hsu, Y.C., Lin, H.F., 2007. Risk analysis for dam overtopping—Feitsui reservoir as a case study. J. Hydraul. Eng. 133 (8), 955–963.
Ladanyi, B., 2002. Behavior of ice/rock mixtures on slopes. In: Merrill, K.S. (Ed.), 11th International Conference on Cold Regions Engineering. Anchorage, Alaska, USA, pp. 683–699.
Leinss, S., Bernardini, E., Jacquemart, M., Dokukin, M., 2021. Glacier detachments and rock-ice avalanches in the Petra Pervogo range, Tajikistan (1973–2019). Nat. Hazards Earth Syst. Sci. 21 (5), 1409–1429.
Li, W., Zhao, B., Xu, Q., Scaringi, G., Lu, H., Huang, R., 2022. More frequent glacier-rock avalanches in Sedongpu gully are blocking the Yarlung Zangbo River in eastern Tibet. Landslides 1–13.
Li, Y., Cui, Y., Hu, X., Lu, Z., Guo, J., Wang, Y., et al., 2024. Glacier retreat in Eastern Himalaya drives catastrophic glacier hazard chain. Geophys. Res. Lett. 51 (8), e2024GL108202.
Lipovsky, P.S., Evans, S.G., Clague, J.J., Hopkinson, C., Couture, R., Bobrowsky, P., et al., 2008. The July 2007 rock and ice avalanches at Mount Steele, St. Elias Mountains, Yukon, Canada. Landslides 5, 445–455.
Liu, J., Cui, Y., Liu, X., Chang, D., 2020. Dynamic characteristics of warm frozen soil under direct shear test-comparison with dynamic triaxial test. Soil Dyn. Earthq. Eng. 133, 106114.
Liu, D., Cui, Y., Wang, H., Jin, W., Wu, C., Bazai, N.A., et al., 2021. Assessment of local outburst flood risk from successive landslides: case study of Baige landslide-dammed lake, upper Jinsha river, eastern Tibet. J. Hydrol. 599, 126294.
Lukas, S., 2005. A test of the englacial thrusting hypothesis of 'hummocky'moraine formation: case studies from the northwest Highlands, Scotland. Boreas 34 (3), 287–307.
Mangold, N., Allemand, P., Duval, P., Geraud, Y., Thomas, P., 2002. Experimental and theoretical deformation of ice–rock mixtures: implications on rheology and ice content of Martian permafrost. Planet. Space Sci. 50 (4), 385–401.
Moore, P.L., 2014. Deformation of debris-ice mixtures. Rev. Geophys. 52 (3), 435–467.
Pudasaini, S.P., Krautblatter, M., 2014. A two-phase mechanical model for rock-ice avalanches. J. Geophys. Res.: Earth Surf. 119 (10), 2272–2290.
Pudasaini, S.P., Krautblatter, M., 2021. The mechanics of landslide mobility with erosion. Nat. Commun. 12 (1), 6793.
Pudasaini, S.P., Mergili, M., 2019. A multi-phase mass flow model. J. Geophys. Res. Earth. Surf. 124 (12), 2920–2942.
Pudasaini, S.P., 2022. Unified mechanical erosion model for multi-phase mass flows. arXiv. 2209.10880.
Pudasaini, S.P., 2024. A multi-phase thermo-mechanical model for rock-ice avalanche. arXiv. 2404.06130.
Paul, F., 2019. Repeat glacier collapses and surges in the Amney Machen Mountain range, Tibet, possibly triggered by a developing rock-slope instability. Remote Sens. 11 (6), 708.
Piciullo, L., Calvello, M., Cepeda, J.M., 2018. Territorial early warning systems for rainfall-induced landslides. Earth Sci. Rev. 179, 228–247.
Schneider, D., Huggel, C., Haeberli, W., Kaitna, R., 2011. Unraveling driving factors for large rock–ice avalanche mobility. Earth Surf. Proc Land 36 (14), 1948–1966.
Shang, Y., Yang, Z., Li, L., Liao, Q., Wang, Y., 2003. A super-large landslide in Tibet in 2000: background, occurrence, disaster, and origin. Geomorphology 54 (3–4), 225–243.
Shugar, D.H., Jacquemart, M., Shean, D., Bhushan, S., Upadhyay, K., Sattar, A., et al., 2021. A massive rock and ice avalanche caused the 2021 disaster at Chamoli, Indian Himalaya. Science 373 (6552), 300–306.
Siddique, T., Haris, P.M., Pradhan, S.P., 2022. Unraveling the geological and meteorological interplay during the 2021 Chamoli disaster, India. Nat. Hazard. Res. 2 (2), 75–83.
Sosio, R., 2015. Rock–snow–ice avalanches. In: Shroder, J.F., Davies, T. (Eds.), Landslide Hazards, Risks, and Disasters. Elsevier, Netherlands, pp. 191–240.

AMS.
Song, C., Huang, B., Richards, K., Ke, L., Hien Phan, V., 2014. Accelerated lake expansion on the Tibetan Plateau in the 2000s: induced by glacial melting or other processes? Water Resour. Res. 50 (4), 3170–3186.
Springman, S.M., Jommi, C., Teysseire, P., 2003. Instabilities on moraine slopes induced by loss of suction: a case history. Geotechnique 53 (1), 3–10.
Suwa, H., Mizuno, T., Ishii, T., 2010. Prediction of a landslide and analysis of slide motion with reference to the 2004 Ohto slide in Nara, Japan. Geomorphology 124 (3–4), 157–163.
Tang, L., Lu, Z., Zheng, J., Zheng, J., Jin, L., Yu, Y., et al., 2023. Mechanism of strength degradation of frozen soil–rock mixture under temperature rise-induced particle ice film melting. Permafrost. Periglac. 34 (4), 530–546.
Tsaparas, I., Rahardjo, H., Toll, D.G., Leong, E.C., 2002. Controlling parameters for rainfall-induced landslides. Comput. Geotech. 29 (1), 1–27.
Tingsanchali, T., Chinnarasri, C., 2001. Numerical modelling of dam failure due to flow overtopping. Hydrol. Sci. J. 46 (1), 113–130.
van der Woerd, J., Owen, L.A., Tapponnier, P., Xiwei, X., Kervyn, F., Finkel, R.C., Barnard, P.L., 2004. Giant,~ M8 earthquake-triggered ice avalanches in the eastern Kunlun Shan, northern Tibet: characteristics, nature and dynamics. Geol. Soc. Am. Bull. 116 (3–4), 394–406.
Wang, H., Cui, P., Li, Y., Tang, J., Wei, R., Yang, A., et al., 2024. Rock and ice avalanche-generated catastrophic debris flow at Chamoli, 7 February 2021: new insights from the geomorphic perspective. Geomorphology, 109110.
Wu, M., Zhou, F., Wang, J., 2023. DEM modeling of mini-triaxial test on soil-rock mixture considering particle shape effect. Comput. Geotech. 153, 105110.
Wu, C., Hu, K., Liu, W., Wang, H., Hu, X., Zhang, X., 2020. Morpho-sedimentary and stratigraphic characteristics of the 2000 Yigong River landslide dam outburst flood deposits, eastern Tibetan Plateau. Geomorphology 367, 107293.
Xiao, Y., Liu, H., Chen, Y., Zhang, W., 2014. Particle size effects in granular soils under true triaxial conditions. Geotechnique 64 (8), 667–672.
Xu, Q., Shang, Y., van Asch, T., Wang, S., Zhang, Z., Dong, X., 2012. Observations from the large, rapid Yigong rock slide–debris avalanche, southeast Tibet. Can. Geotech. J. 49 (5), 589–606.
Yin, Y., Xing, A., 2012. Aerodynamic modeling of the Yigong gigantic rock slide-debris avalanche, Tibet, China. Bull. Eng. Geol. Environ. 71, 149–160.
Zhang, G., Xie, H., Kang, S., Yi, D., Ackley, S.F., 2011. Monitoring lake level changes on the Tibetan Plateau using ICESat altimetry data (2003–2009). Remote Sens. Environ. 115 (7), 1733–1742.
Zhang, T., Gao, Y., Li, B., Yin, Y., Liu, X., Gao, H., Yang, W., 2023a. Characteristics of rock-ice avalanches and geohazard-chains in the Parlung Zangbo Basin, Tibet, China. Geomorphology 422, 108549.
Zhang, T., Wang, W., Shen, Z., Zhan, N., Wang, Z., An, B., 2023b. Understanding the 2004 glacier detachment in the Amney Machen Mountains, northeastern Tibetan Plateau, via multi-phase modeling. Landslides 20 (2), 315–330.
Zhang, J., Zhou, B., Cao, X., Weisai, L., 2019. Analysis of basic characteristics of glacial collapse chain hazards in Animaqing Mountain. Yellow River 41 (11), 17–21 (in Chinese).
Zhong, Q., Chen, S., Fu, Z., 2019. Failure of concrete-face sand-gravel dam due to water flow overtops. J. Perform. Constr Fac. 33 (2), 04019007.
Zhou, J., Cui, P., Hao, M., 2016. Comprehensive analyses of the initiation and entrainment processes of the 2000 Yigong catastrophic landslide in Tibet, China. Landslides 13, 39–54.
Zou, C., Jansen, J.D., Carling, P.A., Dou, X., Wei, Z., Fan, X., 2023. Triggers for multiple glacier detachments from a low-angle valley glacier in the Amney Machen Range, eastern Tibetan Plateau. Geomorphology 440, 108867.

Wenbin Chang is currently pursuing his Joint PhD degree in Civil Engineering at Shanghai Jiao Tong University, China, and Monash University, Australia. He received his BEng degree in Geological Engineering from China University of Mining and Technology in 2018. His areas of research interest include large-scale geohazard modeling, mechanism analysis, and risk assessment, via methods such as DEM, SPH, and laboratory experiments. His PhD thesis work focuses on the initiation mechanism and propagation behavior of rock-ice avalanches in high-latitude mountainous areas.